



## Optimal control strategies for hydrogen production when coupling solid oxide electrolyzers with intermittent renewable energies



Qiong Cai <sup>a,\*</sup>, Claire S. Adjiman <sup>b</sup>, Nigel P. Brandon <sup>c</sup>

<sup>a</sup> Department of Chemical and Process Engineering, University of Surrey, Guildford GU2 7XH, UK

<sup>b</sup> Department of Earth Science and Engineering, Imperial College London, SW7 2AZ, UK

<sup>c</sup> Department of Chemical Engineering, Imperial College London, SW7 2AZ, UK

### HIGHLIGHTS

- Optimal control strategies for renewable hydrogen production are studied.
- A 1D dynamic solid oxide electrolyser model is coupled with a compressor model.
- The effects of electricity input from intermittent renewable energies are examined.
- Three different control strategies are investigated, with relative merits revealed.
- The energy consumption of the SOE system is around 35 kWh per kg H<sub>2</sub>.

### ARTICLE INFO

#### Article history:

Received 9 April 2014

Received in revised form

30 May 2014

Accepted 5 June 2014

Available online 14 June 2014

#### Keywords:

Hydrogen production

Intermittent renewable energies

Solid oxide electrolyzers

Dynamic model

Optimal control

### ABSTRACT

The penetration of intermittent renewable energies requires the development of energy storage technologies. High temperature electrolysis using solid oxide electrolyser cells (SOECs) as a potential energy storage technology, provides the prospect of a cost-effective and energy efficient route to clean hydrogen production. The development of optimal control strategies when SOEC systems are coupled with intermittent renewable energies is discussed. Hydrogen production is examined in relation to energy consumption. Control strategies considered include maximizing hydrogen production, minimizing SOEC energy consumption and minimizing compressor energy consumption. Optimal control trajectories of the operating variables over a given period of time show feasible control for the chosen situations. Temperature control of the SOEC stack is ensured via constraints on the overall temperature difference across the cell and the local temperature gradient within the SOEC stack, to link materials properties with system performance; these constraints are successfully managed. The relative merits of the optimal control strategies are analyzed.

© 2014 Elsevier B.V. All rights reserved.

### 1. Introduction

Renewable energy resources have undergone spectacular development in recent years, to reduce our dependence on fossil fuels and to mitigate its associated pollutant gas emissions and climate change. The existing worldwide renewable power capacity reached about 1470 GW in 2012, up almost 8.5% from 2011. In particular, the total global wind energy capacity and solar photovoltaic (PV) capacity reached 293 GW and 100 GW respectively in 2012, being three times the installed wind capacity and ten times the PV capacity, respectively, that was available just five years

earlier [1]. An electricity system based on intermittent renewable energy sources, such as solar, wind, hydropower, geothermal and marine, gives rise to new challenges concerning the storage and utilization of surplus energy, system operation, energy supply reliability, and future integration with an electrified automotive sector. Energy storage is essential to help cope with these challenges and facilitate a faster penetration of intermittent energy resources. Alongside the several proposed energy storage technologies such as thermal energy storage, battery and supercapacitor storage, energy storage in the form of hydrogen is becoming of increasing interest.

Among the many hydrogen production techniques, water electrolysis is probably the cleanest when combined with a renewable energy source to produce high purity hydrogen. Although commercially available, low temperature water electrolysis based

\* Corresponding author. Tel.: +44 (0)1483686561.

E-mail addresses: [q.cai@surrey.ac.uk](mailto:q.cai@surrey.ac.uk), [q.cai@imperial.ac.uk](mailto:q.cai@imperial.ac.uk) (Q. Cai).

on alkaline and proton exchange membrane (PEM) electrolyzers has not had a significant penetration, mainly due to its high electricity consumption and the challenges arising from cycling when coupled with renewables. High temperature (500–1000 °C) electrolysis for hydrogen production using a solid oxide electrolysis cell (SOEC) appears to be a promising technique because it offers reduced electrical energy consumption per unit of hydrogen compared to low temperature electrolysis due to the favourable combination of thermodynamics and kinetics at high temperatures [2,3].

An SOEC can be seen as the reverse of a solid oxide fuel cell (SOFC), implying that the development of SOEC technology can take advantage of SOFC technology development. However, the underlying electrochemical mechanisms in an SOEC and an SOFC are likely to be different, as is the operation and application context. In fact, experimental testing of SOFC cells under an SOEC operating mode has revealed degradation that is not observed with the SOFC operating mode. [4] This has driven experimental research towards understanding the microstructure and operational effects, as well as developing new materials and stack designs to deal with strong reducing/oxidising environment at high operational temperature [5–13]. Computational models have also been developed, aimed at understanding SOEC performance in relation to operating conditions and material properties, and also to assist the optimization of SOEC performance. These computational models are mostly based on physical and chemical descriptions of the SOEC device itself. These include: (1) the zero-dimensional (0D) steady state isothermal model of a cell developed by Ni et al. [14] to predict the steady-state electrochemical behaviour; (2) the one-dimensional (1D) models developed by Grondin et al. [15] to predict the steady-state voltage–current (V–I) behaviour and the temperature distribution in a cell, and Udagawa et al. [16,17] to predict the dynamic behaviour of the voltage and temperature of an SOEC stack; (3) the two-dimensional (2D) steady-state model of a single repeating unit of a stack developed by Laurencin et al. [18] to predict V–I behaviour and distributions of temperature, heat fluxes, local current densities and gas concentrations; and (4) the three-dimensional (3D) computational fluid dynamics (CFD) model of a multi-cell stack developed by Hawkes et al. [19] to compute spatial-distributed steady-state profiles of temperature, electrical potential and gas composition.

The control strategy used during operation is an important element which should be taken into account when designing and defining the operational characteristics of the SOEC system. It is even more important when the SOEC system is coupled with intermittent energy resources for hydrogen production, due to the time-varying nature of such energy sources. Although a limited number of system optimization studies have been carried out to investigate control strategies for SOFC systems (which may include a fuel cell stack, a fuel processing unit or reformer, air compressor, regulating pressure valves, heat exchangers etc.) [20–23], to the authors' knowledge there has not been such a study for SOEC systems. The only system-level modelling study for the SOEC system was reported by O'Brien et al. [24] who presented a techno-economic analysis of the SOEC system in the context of its coupling with nuclear power to explore the feasibility of different system configurations. For such studies, lumped-parameter models are often used to represent the behaviour of the devices involved.

In this paper, we present our preliminary results on the identification of optimal control strategies for the operation of SOEC systems to offer efficient large-scale operation. Three different control objectives relevant to system operation are investigated and discussed. The objective of this study is to examine hydrogen production in relation to energy consumption, whilst maintaining control over the SOEC stack temperature distribution, by employing

a 1D dynamic SOEC stack model [17] within the overall system model, to allow a detailed examination of the performance of the stack. The description of the system model and the optimal control strategies are given in the next section, followed by results and discussions in Section 3. Conclusions from this study are given in Section 4.

## 2. Methodology

A complete SOEC system has to include an energy source to provide the electrical input, an SOEC stack as the core part, and a number of auxiliary devices (e.g., compressor, reactant flow regulator, heat exchanger, steam/hydrogen separator, thermal management unit, power management unit). Precise control of the whole system is critical to the viability, efficiency and robustness of the SOEC system. However, development of control strategies for the whole system is a complex and computationally expensive task, as it requires models for all the devices involved, to explore quantitatively the interactions and trade-offs between the different units.

The aim of this study is to examine hydrogen production in relation to energy consumption. Two system components dominate the energy consumption of the system, the SOEC stack and the air compressor (when it is used to blow air for temperature control [22]). As such, a simplified SOEC system model is explored here to include an SOEC model and a compressor model, as depicted in Fig. 1. A 1D dynamic SOEC model previously developed [17] is employed to allow the detailed examination of the hydrogen production associated with different operating conditions, and the control of the operation of the SOEC. Particularly, temperature control of the SOEC stack is only possible using a dynamic SOEC model of at least 1D, as it allows the temperature gradient within the cell to be examined, and enables temperature control to avoid thermal excursion and cell failure. The electrical input is allowed to vary over time to represent the coupling of the SOEC system with intermittent energy resources.

Detailed descriptions of the 1D dynamic SOEC model and the air compressor model are given in this section, together with explanations of the control strategies studied. The advantages and disadvantages of each strategy are also discussed.

Note that in this paper, we model a single unit cell in the middle of an SOEC stack to represent the performance of the stack, neglecting end effects. Therefore, air flow from the compressor and the electricity input to the system are tailored for a unit cell, as are the hydrogen production and energy consumption results to be reported later. This has the benefit of having a representative case study which is not limited by the size of the system, so that the values (particularly, hydrogen production and energy consumption) reported in this paper can easily be scaled to systems of any size, based on the number of the cells in the SOEC stack, assuming that every cell in the stack gives the same performance.

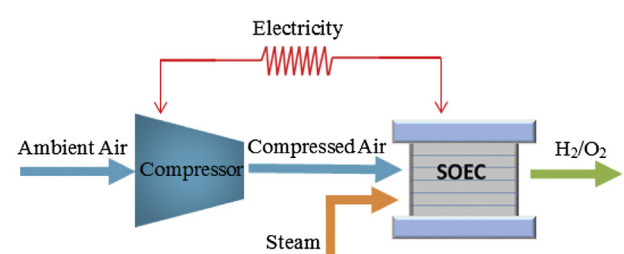


**Fig. 1.** Schematic illustration of the SOEC system which includes an SOEC stack for hydrogen production and an air compressor to provide air for temperature control of the SOEC stack.

## 2.1. Description of the 1D dynamic SOEC model

The 1D dynamic SOEC model developed is used to simulate a unit cell in the centre of a sufficiently large stack, so as to represent the performance of an SOEC stack. A schematic view of such a unit cell is shown in Fig. 2. A planar SOEC stack contains a number of repeating cells to achieve a sufficient hydrogen production rate. Each individual cell consists of a three-layer solid structure (composed of porous cathode, electrolyte and porous anode) and an interconnect plate. The gas channels are embedded in the interconnect. Steam is introduced at the cathode side of the solid structure where it is reduced to hydrogen, releasing oxide ions in the process. The oxide ions then migrate through the electrolyte to the anode where they combine to form oxygen molecules, releasing electrons. For modelling purposes, the unit cell is considered to consist of four components, the cathode and anode gas streams, the solid structure and the interconnect. All the gases involved are assumed ideal. The cathode stream inlet gas is composed of 10% mole H<sub>2</sub> and 90% mole H<sub>2</sub>O. The addition of hydrogen in the cathode stream mitigates the oxidation of materials that might be induced by using pure steam. On the anode side, air (modelled as a mixture of 21% mole O<sub>2</sub> and 79% mole N<sub>2</sub>) is introduced concurrently with the cathode stream to enable temperature control of the stack. The stack is designed to operate around 1073 K [3,4]; the temperature variation that occurs during stack operation is controlled by introducing hot air ( $T = 1073$  K) on the anode side and manipulating the air flow rate, as indicated in Section 2.1.4. Please note that the exact nature of the heat supply is not considered in this study; we assume that waste heat from a separate process is used. The operating pressure is  $1.2 \times 10^5$  Pa. The inlet flow rate of the cathode stream is  $f_c^0 = 2 \times 10^{-3}$  mol s<sup>-1</sup> which is equivalent to 8920 ml min<sup>-1</sup>.

The model is used to simulate a cell with dimensions of 10 cm  $\times$  10 cm in the  $x$  and  $y$  directions, with variations in the  $y$  direction, perpendicular to the flow direction, being ignored. The  $z$  direction gives the heights of the cell components and also the height of the whole stack. A detailed description of the cell geometry and material properties can be found in Appendix [25]. The equations are developed and solved along the  $x$  direction. The results to be presented are normalized along the cell length, with  $x = 0$  indicating the inlet and  $x = 1$  indicating the outlet.

The model developed consists of an electrochemical model, mass balances for the gas streams, and energy balances for the cathode and anode streams, solid structure and interconnect. The equations are given in Tables 1–3, and the nomenclature can be found at the end of this paper.

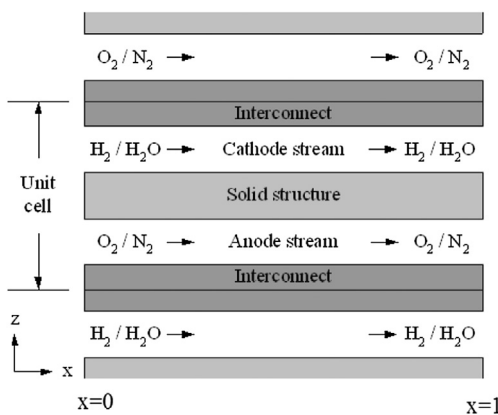


Fig. 2. Schematic view of a unit cell of a planar SOEC stack.

### 2.1.1. Electrochemical model

An electrochemical model relates variables such as gas species concentrations, cell component temperatures and average current density to the electrical potential of the cell, which can then be used to calculate the electrical energy consumption. The cell potential corresponds to the sum of the reversible potential and all the irreversible losses that occur as the electrical current passes through the cell. Irreversible losses consist of cathode and anode activation overpotentials, cathode and anode concentration overpotentials and ohmic losses. These irreversible losses are partly responsible for the heat produced within the cell. Mathematical descriptions of the electrochemical model are given in Table 1.

### 2.1.2. Mass balances

The mass balances represent the gas flow behaviour inside the cathode and anode. The mass balance equations are based on the mass conservation principle, and the thermodynamic properties of gas mixtures. The composition of the cathode stream changes along the cell, and is taken into account in the model using the cathode stream mass balances and boundary conditions at the cell inlet, which allows the prediction of hydrogen and water concentrations at each position along the channel. For the anode stream, mass balances and boundary conditions at the inlet predict the O<sub>2</sub> and N<sub>2</sub> concentrations at each position along the cell. Mathematical descriptions of the mass balances are given in Table 2.

### 2.1.3. Energy balances

Energy balances are a key driver to predict the temperature distribution along the cathode and anode streams, solid structure and interconnect. Heat exchange between the gas streams and walls (solid part of the cells) is fully described by convection. The thermal fluxes along the solid parts of the cell can be modelled using Fourier's law of heat conduction while taking into account the radiative heat exchange between walls and interconnect. Mathematical descriptions of the energy balances are given in Table 3.

### 2.1.4. Temperature control

Temperature control is provided for the SOEC stack through manipulation of the air ratio on the anode side. The air ratio provides a measure of the inlet flow rate of air in relation to the rate of reaction. It is defined as the ratio between the molar flow rate of O<sub>2</sub> in the inlet air flow to the number of moles of O<sub>2</sub> produced in the unit cell, per unit time. The mathematical expression for the air ratio,  $\psi$ , is

$$\psi = \frac{2F_A^0(t)y_{O_2}(0, t)}{\bar{j}(t)Lw\nu_{O_2}}, \quad t \in \{0, t_f\} \quad (1)$$

As indicated by Eq. (1), the inlet flow rate of the anode stream  $f_A^0$  is co-determined by the air ratio and operating current density, and varies with operating conditions.

## 2.2. The compressor model

The compressor model in this study is a simple steady-state model which links the air compressor power to the air stream flow rate,  $\dot{m}_{air}$ , and temperature,  $T$ , the calorific properties of air (i.e.  $c_p$  and  $\gamma$ ), and the inlet and outlet of the pressure through the compressor.

The parasitic power required by the air compressor, which supplies the total amount of air needed to meet the stack cooling requirement, is modelled as follows [22]:

**Table 1**

The dynamic SOEC model: electrochemical model.

<b>Cell working potential:</b> $U(t) = U^{\text{rev}}(x, t) + \eta_{\text{Ohm}}(x, t) + \eta_{\text{conc,cathode}}(x, t) + \eta_{\text{conc,anode}}(x, t) + \eta_{\text{act,cathode}}(x, t) + \eta_{\text{act,anode}}(x, t)$ , $t \in [0, t_f]$
<b>Reversible potential:</b> $U^{\text{rev}}(x, t) = U^0(x, t) + \frac{\Re T_S(x, t)}{2F} \ln \left( \frac{C_{H_2}(x, t)(p_{O_2}(t) \times 10^{-5})^{0.5}}{C_{H_2O}(x, t)} \right)$ , $t \in [0, t_f]$
<b>Ohmic loss:</b> $\eta_{\text{Ohm}}(x, t) = j(x, t)$ , $R_{\text{Ohm}}(x, t)R_{\text{Ohm}}(x, t) = \frac{\tau_{\text{cathode}}}{\sigma_{\text{cathode}}} + \frac{\tau_{\text{electrolyte}}}{\sigma_{\text{electrolyte}}(x, t)} + \frac{\tau_{\text{anode}}}{\sigma_{\text{anode}}}$ , $t \in [0, t_f]$
<b>Concentration overpotential:</b> $\eta_{\text{conc,cathode}}(x, t) = \frac{\Re T_S(x, t)}{2F} \ln \left( \frac{C_{H_2}^{\text{TPB}}(x, t)C_{H_2O}(x, t)}{C_{H_2}(x, t)C_{H_2O}^{\text{TPB}}(x, t)} \right)$ ; $\eta_{\text{conc,anode}}(x, t) = \frac{\Re T_S(x, t)}{4F} \ln \left( \frac{C_{O_2}^{\text{TPB}}(x, t)T_S(x, t)}{C_{O_2}(x, t)T_A(x, t)} \right)$
$C_{H_2}^{\text{TPB}}(x, t) = C_{H_2}(x, t) + \frac{\tau_{\text{cathode}}}{2FD_{\text{eff,cathode}}} j(x, t)$ ; $C_{H_2O}^{\text{TPB}}(x, t) = C_{H_2O}(x, t) - \frac{\tau_{\text{cathode}}}{2FD_{\text{eff,cathode}}} j(x, t)$
$C_{O_2}^{\text{TPB}}(x, t) = C_{O_2}(x, t) + C_{N_2}(x, t) - C_{N_2}(x, t) \exp \left( \frac{-j(x, t)\tau_{\text{anode}}}{4FD_{\text{eff,anode}}[C_{O_2}(x, t) + C_{N_2}(x, t)]} \right)$ , $t \in [0, t_f]$
<b>Activation overpotential:</b>
$j(x, t) = j_{0, \text{cathode}}(x, t) \left[ \frac{C_{H_2}^{\text{TPB}}(x, t)}{C_{H_2}(x, t)} \exp \left( \frac{2(1-\alpha)F}{\Re T_S(x, t)} \eta_{\text{act,cathode}}(x, t) \right) - \frac{C_{H_2O}^{\text{TPB}}(x, t)}{C_{H_2O}(x, t)} \exp \left( \frac{-2\alpha F}{\Re T_S(x, t)} \eta_{\text{act,cathode}}(x, t) \right) \right]$ , $t \in [0, t_f]$
$j(x, t) = j_{0, \text{anode}}(x, t) \left[ \exp \left( \frac{2(1-\alpha)F}{\Re T_S(x, t)} \eta_{\text{act,anode}}(x, t) \right) - \frac{C_{O_2}^{\text{TPB}}(x, t)}{C_{O_2}(x, t)} \exp \left( \frac{-2\alpha F}{\Re T_S(x, t)} \eta_{\text{act,anode}}(x, t) \right) \right]$ , $t \in [0, t_f]$
$j_{0, \text{electrode}}(x, t) = \frac{\Re T_S(x, t)}{2F} k_{\text{electrode}} \exp \left[ \frac{-E_{\text{electrode}}}{\Re T_S(x, t)} \right]$ , electrode $\in \{\text{cathode, anode}\}$ , $t \in [0, t_f]$

**Table 2**

The dynamic SOEC model: mass balances.

<b>Cathode stream mass balance</b>
$\frac{\partial}{\partial t}[C_i(x, t)] = -u_{C\bar{\alpha}X}[C_i(x, t)] + \frac{1}{h_c} \nu_i R(x, t)$ , $i \in \{\text{H}_2, \text{H}_2\text{O}\}$ , $t \in [0, t_f]$
$C_i(0, 0) = C_i^0$ , $i \in \{\text{H}_2, \text{H}_2\text{O}\}$
$R(x, t) = \frac{j(x, t)}{2F}$ , $t \in [0, t_f]$
<b>Anode stream mass balance</b>
$\frac{\partial}{\partial t}[C_i(x, t)] = -u_{A\bar{\alpha}X}[C_i(x, t)] + \frac{1}{h_a} \nu_i R(x, t)$ , $i \in \{\text{O}_2, \text{N}_2\}$ , $t \in [0, t_f]$
$C_i(0, 0) = C_i^0$ , $i \in \{\text{O}_2, \text{N}_2\}$ , $t \in [0, t_f]$

$$P_{\text{CP}}(t) = \dot{m}_{\text{air}}(t) \frac{C_{P, \text{air}} T(t)}{\eta_{\text{EM}} \eta_{\text{CP}}} \left[ \left( \frac{p_{\text{out}}(t)}{p_{\text{in}}(t)} \right)^{(\gamma-1)/\gamma} - 1 \right], \quad t \in \{0, t_f\} \quad (2)$$

The inlet air pressure  $p_{\text{in}}$  is equal to the ambient pressure of  $1.0 \times 10^5$  Pa. The outlet air pressure  $p_{\text{out}}$  is equal to the operating pressure of the SOEC stack, which in this case is  $1.2 \times 10^5$  Pa. This gives a compression ratio  $p_{\text{out}}/p_{\text{in}} = 1.2$ .

The air mass flow rate  $\dot{m}_{\text{air}}$  in Eq. (2) is linked to the inlet flow rate of the anode stream  $f_A^0(t)$  in the SOEC by adding the density

factor of air  $\rho_{\text{air}}$  and the molar volume ( $RT/P$ ) for the purpose of unit conversion.

$$\dot{m}_{\text{air}}(t) = \rho_{\text{air}}(T, P) f_A^0(t) \frac{RT}{P} \quad (3)$$

### 2.3. Optimal control strategies

The development of suitable optimal control strategies for the SOEC system relies on an understanding of the characteristics of both the SOEC system and the coupled electricity supply. Two scenarios are considered in this study.

- The heating and cooling of an SOEC stack, during which the current density is a manipulated variable.
- The SOEC system is integrated with an intermittent source of energy, during which the electrical energy input is treated as a disturbance.

In Scenario A, the optimal control unit is used to set, within a given range of current densities, the current density at which the

**Table 3**

The dynamic SOEC model: energy balances.

<b>Cathode stream</b>
$\frac{\partial}{\partial t}[T_C(x, t)] = -u_{C\bar{\alpha}X}[T_C(x, t)] + \frac{k_c}{\rho_c c_{p,c} h_c} [T_S(x, t) - T_C(x, t)] + \frac{k_c}{\rho_c c_{p,c} h_c} [T_l(x, t) - T_C(x, t)]$ , $t \in [0, t_f]$
$T_C(0, 0) = T_C^0$ , $k_c = Nu_{C\bar{\alpha}X} \frac{\lambda_c}{d_{h,c}}$ , $d_{h,c} = \frac{2Wh_c}{W+h_c}$ , $t \in [0, t_f]$
<b>Anode stream</b>
$\frac{\partial}{\partial t}[T_A(x, t)] = -u_{A\bar{\alpha}X}[T_A(x, t)] + \frac{k_a}{\rho_a c_{p,a} h_a} [T_S(x, t) - T_A(x, t)] + \frac{k_a}{\rho_a c_{p,a} h_a} [T_l(x, t) - T_A(x, t)]$ , $t \in [0, t_f]$
$T_A(0, 0) = \frac{T_C(0, 0) + T_l(0, 0)}{2}$ , $k_a = Nu_{A\bar{\alpha}X} \frac{\lambda_a}{d_{h,a}}$ , $d_{h,a} = \frac{2Wh_a}{W+h_a}$ , $t \in [0, t_f]$
<b>Solid structure</b>
$\frac{\partial}{\partial t}[T_S(x, t)] = \frac{\lambda_s}{\rho_s c_{p,s}} \frac{\partial^2}{\partial x^2} [T_S(x, t)] - \frac{k_s}{\rho_s c_{p,s} h_s} [T_S(x, t) - T_C(x, t)] - \frac{k_s}{\rho_s c_{p,s} h_s} [T_S(x, t) - T_A(x, t)] - \frac{2}{\rho_s c_{p,s} h_s} \left[ \frac{\sigma [T_S(x, t)^4 - T_l(x, t)^4]}{1/\varepsilon_s + 1/\varepsilon_l - 1} \right] + \frac{1}{\rho_s c_{p,s} h_s} [-\Delta H(x, t)R(x, t) + j(x, t)U(t)]$ , $t \in [0, t_f]$
$\frac{\partial}{\partial x}[T_S(0, 0)] = 0$ , $\frac{\partial}{\partial x}[T_S(1, 0)] = 0$ , $t \in [0, t_f]$
<b>Interconnect</b>
$\frac{\partial}{\partial t}[T_l(x, t)] = \frac{\lambda_l}{\rho_l c_{p,l}} \frac{\partial^2}{\partial x^2} [T_l(x, t)] - \frac{k_l}{\rho_l c_{p,l} h_l} [T_l(x, t) - T_C(x, t)] - \frac{k_l}{\rho_l c_{p,l} h_l} [T_l(x, t) - T_A(x, t)] + \frac{2}{\rho_l c_{p,l} h_l} \left[ \frac{\sigma [T_S(x, t)^4 - T_l(x, t)^4]}{1/\varepsilon_s + 1/\varepsilon_l - 1} \right]$ , $t \in [0, t_f]$
$\frac{\partial}{\partial x}[T_l(0, 0)] = 0$ , $\frac{\partial}{\partial x}[T_l(1, 0)] = 0$ , $t \in [0, t_f]$

**Table 4**

Mathematical descriptions of optimal control strategies.

Representative scenarios	Optimization objective	Constraints	Control variables
A. Heating and cooling	<p>(a) Maximizing hydrogen production</p> $Y_{H_2,\text{total}} = \int_{t=0}^{t=t_f} \dot{Y}_{H_2}(t) dt = f_C^1(t)C_{H_2}(1, t) - f_C^0(t)C_{H_2}(0, t)$ <p>(b) Minimizing SOEC energy consumption</p> $E_{\text{SOEC}} = \int_{t=0}^{t=t_f} P_{\text{SOEC}}(t) dt = U(t)\bar{j}(t)$	Path constraints 1 Acceptable temperature gradients across entire SOEC $ \Delta T_C(t)  =  T_C(1, t) - T_C(0, t)  \leq 100K, t \in [0, t_f]$ 2 Acceptable local temperature gradients $ \partial T_S(x, t)/\partial x  \leq 10K, t \in [0, t_f]$ 3 Limiting power to compressor $0 < P_{CP}(t) < P_{CP\text{max}}, t \in [0, t_f]$ End-point constraints 4 Returning to steady-state $\partial \Delta T_C(t)/\partial t = 0 \text{ at } t = t_f$ Path constraints 1 Acceptable temperature gradients $ \Delta T_C(t)  =  T_C(1, t) - T_C(0, t)  \leq 100K, t \in [0, t_f]$ 2 Acceptable local temperature gradients $ \partial T_S(x, t)/\partial x  \leq 10K, t \in [0, t_f]$ End-point constraints 3 Returning to steady-state $\partial \Delta T_C(t)/\partial t = 0 \text{ at } t = t_f$	<ul style="list-style-type: none"> <li>• Time horizon <math>t_f</math></li> <li>• Air ratio <math>0.4 \leq \psi \leq 14</math></li> <li>• Current density <math>1000 \leq \bar{j} \leq 7000 \text{ A m}^{-2}</math></li> </ul>
B. Electricity disturbance	<p>(c) Minimizing compressor energy consumption</p> $E_{CP} = \int_{t=0}^{t=t_f} P_{CP}(t) dt$	Path constraints 1 Acceptable temperature gradients $ \Delta T_C(t)  =  T_C(1, t) - T_C(0, t)  \leq 100K, t \in [0, t_f]$ 2 Acceptable local temperature gradients $ \partial T_S(x, t)/\partial x  \leq 10K, t \in [0, t_f]$ End-point constraints 3 Returning to steady-state $\partial \Delta T_C(t)/\partial t = 0 \text{ at } t = t_f$	<ul style="list-style-type: none"> <li>• Time horizon <math>t_f</math></li> <li>• Air ratio <math>0.4 \leq \psi \leq 14</math></li> <li>• Total input power <math>20 \leq P_{\text{total}} \leq 100 \text{ W}</math></li> </ul>

SOEC stack should be operating in order to achieve the control objectives. The electrical energy demand in this scenario is thus determined by how the SOEC stack is operated. In Scenario B, however, the electrical energy availability is pre-determined as an input to the SOEC stack; the optimal control unit reacts accordingly under this electricity-input disturbance to achieve the control objectives.

### 2.3.1. Control objectives

Control objectives, which reflect the purposes and functions of a system, can be chosen depending on the specific operating context. Three optimal control situations are considered with different control objectives: (a) maximizing hydrogen production, (b) minimizing the electrical energy consumption from the SOEC stack, and (c) minimizing the electrical energy consumption from the air compressor. The first two optimal control situations are studied under Scenario A, whilst the third optimal control situation is studied under Scenario B. For all the control situations considered, certain constraints have to be satisfied in order to keep the system working. This is further discussed in the next sections.

#### 2.3.1.1. Scenario A: heating and cooling

**2.3.1.1.1. Maximizing hydrogen production.** This control strategy may arise when there is abundant electricity available from intermittent energy sources, for instance in the case when the electricity generated exceeds the demand. In this situation, maximizing hydrogen production is desirable so that the surplus electricity can be stored in the form of hydrogen. This control strategy may also be suited when there is a high hydrogen demand in the supply chain. The amount of hydrogen produced is directly dependent on the current density at which the SOEC is operating. As an example, here we set lower and upper bounds on the operational current density range (see Table 4), and let the optimal controller determine how the SOEC should be operating, in accordance with Scenario A. The objective function for maximizing the hydrogen production of the process over a given time horizon is given in Table 4. The hydrogen production rate,  $\dot{Y}_{H_2}$ , is calculated as the molar flow rate of hydrogen at the outlet of the cathode stream minus the molar flow rate of hydrogen at the inlet of the cathode stream.

**2.3.1.1.2. Minimizing the energy consumption of the SOEC stack.** When the available electricity for hydrogen production is limited or the demand on hydrogen production is low, it is desirable to operate the SOEC system such that the electrical energy

consumption is minimized to reduce the operating cost. As the SOEC stack is one of the main electrical energy consumers in the system, it is therefore necessary to minimize the electrical energy consumption of the SOEC stack. The objective function for minimizing the electrical energy consumption of the SOEC stack within a given time horizon is given in Table 4. The power consumed by the SOEC per unit time  $P_{\text{SOEC}}$  is calculated as the product of the cell voltage and the average current density of the SOEC stack. To compare with case (a) of maximizing hydrogen production, this optimal control situation is studied with the same control variables as (a), where the optimal controller determines how the SOEC should be operating given an operational current density range with fixed lower and upper bounds.

#### 2.3.1.2. Scenario B: electricity disturbance

**2.3.1.2.1. Minimizing electrical energy consumption from air compressor.** Here we consider control under Scenario B where the electrical energy is a disturbance to the system. In this scenario, the possibility of both maximizing hydrogen production and minimizing electrical energy consumption of the SOEC system at the same time is explored. To achieve both objectives simultaneously, the control objective is set to minimize the electrical energy consumption from the air compressor. For a given electricity input, by minimizing the electrical energy consumption of the air compressor, more electrical energy is then available for the SOEC stack which will, in turn, maximize the amount of hydrogen produced. The objective function for minimizing energy consumption from the air compressor is given in Table 4.

#### 2.3.2. Constraints

In optimal control problems it is vital to identify the constraints for a given process, as constraints determine the limit of the feasibility and the flexibility of the process. In the optimal control studies presented in this paper, two kinds of constraints are imposed, namely path constraints, and end-point constraints. Path constraints have to be satisfied at all times during operation, whilst end-point constraints have to be satisfied only at the end of the time horizon. The mathematical forms of the constraints are given in Table 4.

For all the control situations, it is important to ensure that the temperature profile within the SOEC stack satisfies the constraints on the temperature gradients at all times to avoid excessive thermal excursion of the ceramic materials. In previous studies, a

maximum allowable local thermal gradient along the cell (particularly in the solid structure which consists of cathode, electrolyte and anode) has been estimated to be  $10 \text{ K cm}^{-1}$ , and a maximum allowable overall temperature difference along the cathode stream for a cell of 10 cm to be 100 K [26]. Two temperature constraints are thus implemented: the absolute temperature difference  $|\Delta T_C|$  across the 10 cm cell must be less than or equal to 100 K (constraint 1 in Table 4); and the absolute local temperature gradient  $|\partial T_S / \partial x|$  must be less than or equal to  $10 \text{ K cm}^{-1}$  (constraint 2 in Table 4). In addition, an end-point constraint is imposed on the derivative of the overall temperature difference to ensure that the system reaches equilibrium (i.e. no fluctuation) at the end of the operation (constraint 4 in Scenario A and 3 in Scenario B, Table 4).

Furthermore, in Scenario A, considering that the air compressor is one of the main electrical energy consumers, it is also desirable to limit its electrical energy consumption whilst fulfilling the temperature control requirements of the SOEC stack. A path constraint is imposed to provide an upper bound over the electrical energy consumption by the air compressor. Its formulation is shown as constraint 3 in Scenario A. Its effects will be shown and discussed in the results section.  $P_{\max}$  is adjusted according to the system operating conditions, in relation to current density and air flow rate, as indicated by Eqs. (1) and (2). This helps us explore trade-offs with the air compressor power control. If any of the constraints is not satisfied during operation, the process is infeasible.

### 2.3.3. Control variables

In all the optimal control situations considered, the control time horizon,  $t_f$ , is set to be 3000 s. The air ratio, defined as the ratio of the inlet flow rate of air on the anode side to the gas inlet flow rate on the cathode side, is used as a control variable to limit temperature variation. The lower and upper bound for the air ratio are selected to be 0.4 and 14 respectively, considering system constraints [4]. For control situations (a) and (b) where we have control on the operational current density of the SOEC stack, the operating regime for current density is between 1000 and 7000  $\text{A m}^{-2}$ . For control situation (c), where the electrical energy is an input disturbance, various configurations of the electrical power input are selected, allowing the electrical power to vary between 20 and 100 W (for input to a cell) over a time horizon of 3000 s. The mathematical descriptions of the control variables are given in Table 4.

### 2.3.4. Control vector parameterization

Control vector parameterization [27] is used to formulate the optimal control problem. In this approach, control variables are allowed to achieve solutions of a pre-specified functional form, e.g. piecewise constant and piecewise linear controls with continuity at the interval boundaries. The time horizon is discretized into non-uniform time intervals. Two types of parameterization are considered: piecewise-constant controls, for which constant control parameter values are assumed over each interval, and piecewise-linear controls, for which control parameter values with constant positive or negative gradients are assumed over each interval, as illustrated in Fig. 3. More complex forms can also be considered.

The benefit of this approach is that the infinite-dimensional optimal control problem is reduced to an optimization problem in a few variables, e.g. in the case of piecewise constant control, a control variable  $u(t)$  is described by:

$$u(t) = \begin{cases} u_1, & 0 \leq t \leq t_1 \\ u_2, & 0 \leq t \leq t_2 \\ \vdots \\ u_f, & 0 \leq t \leq t_f \end{cases} \quad (4)$$

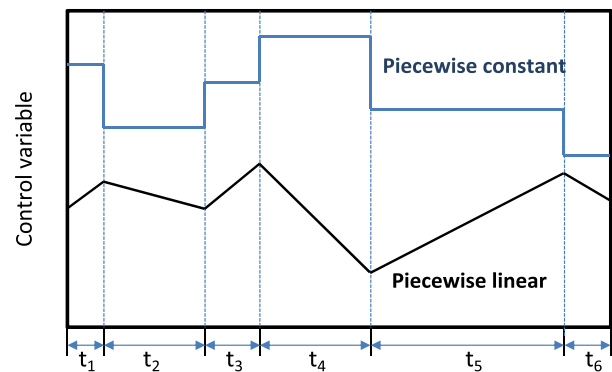


Fig. 3. A schematic of the control variable profiles that can be obtained with control vector parameterization, for piecewise constant and piecewise linear parameterizations.

Both the durations of the time intervals and the values of the control parameters are treated as variables.

The optimal control profiles reported in this paper are obtained with piecewise constant controller; a piecewise linear controller was also investigated, but it does not bring benefits in terms of giving a better solution.

## 3. Results and discussions

The optimal control problems, in which the system of partial differential and algebraic equations for the 1D dynamic SOEC stack model the air compressor model are embedded, are solved under all scenarios via gPROMS Model Builder 3.4.

Before performing optimal control calculations, the steady state performance of the SOEC is investigated to gain a better understanding of the SOEC performance. Fig. 4 shows the operational cell voltage and the open circuit voltage (OCV) over a wide range of operating current densities at 1073 K. When current density increases, the cell voltage also increases, but remains below the thermal-neutral voltage of 1.30 V at 1073 K for the entire range of current densities investigated, featuring endothermic operation. The OCV remains the same over the entire range of operating current densities. When operating at 1000, 7000 and 10,000  $\text{A m}^{-2}$ , a voltage difference (between the operational voltage and the OCV)

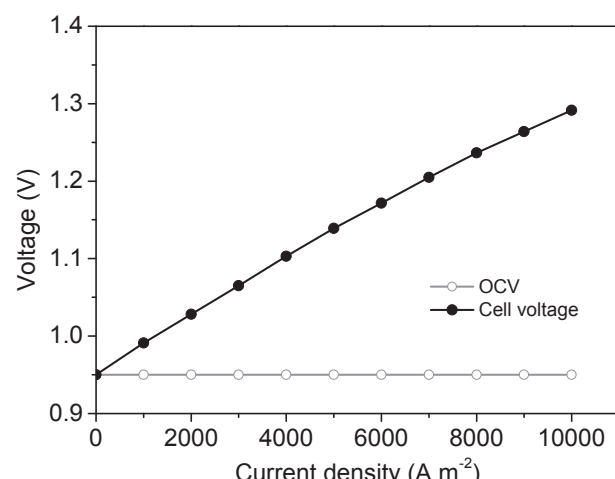
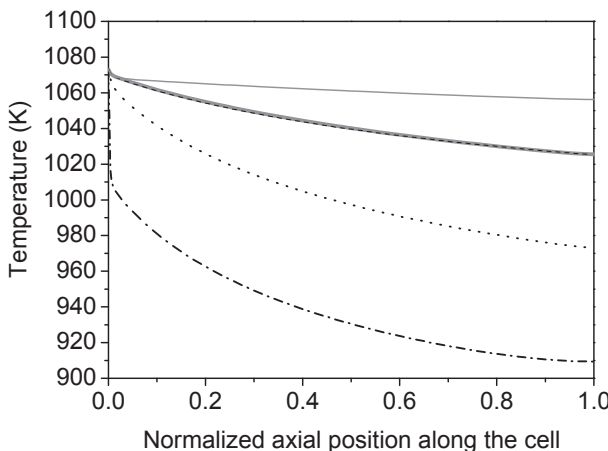


Fig. 4. Operational cell voltage and open circuit voltage (OCV) at a range of current densities.

of 41, 255, and 340 mV is found respectively, indicating the increase of irreversible losses within the cell as current density is increased. The area specific resistance (ASR) calculated is  $0.44 \Omega \text{ cm}^2$  when operating at  $1000 \text{ A m}^{-2}$ , and  $0.36 \Omega \text{ cm}^2$  when operating at  $10,000 \text{ A m}^{-2}$ , showing a gradual decrease of ASR with increasing current density. For Scenario A, where we have control over the average current density  $\bar{j}$  between  $1000$  and  $7000 \text{ A m}^{-2}$ , operations at  $1000$  and  $7000 \text{ A m}^{-2}$  are examined to understand the bounds on the air ratio that can be used to control the system so that the temperature constraints are met. Fig. 5 shows the cathode stream temperature distribution along the cell. As can be seen, the cathode stream temperature decreases along the cell from the inlet (normalized position  $x = 0$ ) to the outlet ( $x = 1$ , corresponding to a length of 10 cm) for all the operating conditions investigated, featuring endothermic operation. When operating at  $1000 \text{ A m}^{-2}$  with a minimum air ratio of 0.4, the temperature gradient between the inlet and the outlet is 164 K, which exceeds the maximum temperature gradient of 100 K allowed for a 10 cm cell, and thus puts the cell in danger of breakdown. A minimum air ratio of 2.71 is required to reduce the temperature gradient, in this case, to 99.3 K. The operation with a maximum air ratio of 14 is also examined, showing that the temperature gradient is maintained at 48 K. When operating at a current density of  $7000 \text{ A m}^{-2}$ , the cell features a temperature gradient of 48 K along the cell with a minimum air ratio of 0.4, and a temperature gradient of 17 K with a maximum air ratio of 14. Based on the monotonic behaviour of the temperature gradient with the air ratio, this means that any air ratio value in the control range of 0.4–14 is sufficient for the temperature control to meet the temperature constraint at higher current densities. From Fig. 4, the initial guess for the optimization studies are set to be: air ratio of 2.71 when operating at current density of  $1000 \text{ A m}^{-2}$ , air ratio of 0.4 when operating at current density of  $7000 \text{ A m}^{-2}$ .

### 3.1. Maximizing hydrogen production

Fig. 6 shows the optimal control profiles in the case of maximizing hydrogen production. To achieve maximum hydrogen production within the control period of 3000 s, current density increases from  $1000$  to  $7000 \text{ A m}^{-2}$  within 5 s at the start of the control period and is maintained at  $7000 \text{ A m}^{-2}$  until the end of the



**Fig. 5.** Cathode stream temperature distribution along the cell. The dash-dotted line indicates operation at  $1000 \text{ A m}^{-2}$  with an air ratio of 0.4. The dotted line indicates operation at  $1000 \text{ A m}^{-2}$  with an air ratio of 2.71. The dashed line indicates operating at  $1000 \text{ A m}^{-2}$  with an air ratio of 14. The thick solid line indicates operating at  $7000 \text{ A m}^{-2}$  with an air ratio of 0.4. The thin solid line indicates operating at  $7000 \text{ A m}^{-2}$  with an air ratio of 14.

control period, as shown in Fig. 6(a). In response to the change in the operating current density, the cumulative amount of hydrogen produced,  $Y_{\text{H}_2,\text{total}}$ , increases linearly with time and reaches a maximum of 1.09 mol.

For operations at current density of  $7000 \text{ A m}^{-2}$ , the implemented upper limit of the compressor power,  $P_{\text{CPmax}}$ , is set to different values in the range of 3.4–120 W to examine the effect of temperature control. These values are calculated based on the operating current density  $\bar{j}$  and air ratio  $\psi$  using Eqs. (1) and (2);  $P_{\text{CPmax}} = 3.4 \text{ W}$  corresponds to  $\bar{j} = 7000 \text{ A m}^{-2}$  and  $\psi = 0.4$ , while  $P_{\text{CPmax}} = 120 \text{ W}$  corresponds to  $\bar{j} = 7000 \text{ A m}^{-2}$  and  $\psi = 14$ . Fig. 6(b) shows how the air ratio responds to the compressor power upper bound: it rises or falls at  $t = 1 \text{ s}$  from the initial value of 2.71 to a constant value corresponding to the maximum compressor power. When  $P_{\text{CPmax}} < 3.4 \text{ W}$ , it is not feasible to control the SOEC as it violates the lower bound of the air ratio value of 0.4; when  $P_{\text{CPmax}} > 120 \text{ W}$ , the optimal control problem is always feasible and the air ratio always stays at the upper bound of the air ratio of 14. Fig. 6(c) shows that the temperature difference between the outlet and inlet of the cell always satisfies the constraint  $|\Delta T_C| \leq 100 \text{ K}$  and reaches steady state towards the end of the control period ( $t = 3000 \text{ s}$ ). The absolute value of the maximum local temperature gradient in the solid structure,  $|\partial T_S(x, t)/\partial x|$  is found to be under the upper limit of 10 K for all the  $P_{\text{CPmax}}$  values studied, as shown in Fig. 6(d). It is also obvious that with a small compressor power limit, the cell operates with a larger temperature difference and the temperature takes longer to stabilize, and vice versa. For example, with  $P_{\text{CPmax}} = 120 \text{ W}$ , a high air ratio of 14 is used so that a comparatively large air flow rate is introduced to the anode stream of the SOEC stack, bringing the initial temperature difference of  $\Delta T_C = -99.3 \text{ K}$  to a final temperature difference of  $\Delta T_C = -16.8 \text{ K}$  within 250 s; with  $P_{\text{CPmax}} = 4 \text{ W}$ , a low air ratio of 0.4 is introduced, bringing the initial temperature difference of  $\Delta T_C = -99.3 \text{ K}$  to a final temperature difference of  $\Delta T_C = -46 \text{ K}$  within 1240 s.

### 3.2. Minimizing the SOEC energy consumption

Fig. 7 shows the optimal control profiles in the case of minimizing the SOEC energy consumption. As shown in Fig. 7(a), current density decreases from  $7000$  to  $1000 \text{ A m}^{-2}$  at the start of the time horizon and remains at  $1000 \text{ A m}^{-2}$  till the end of the control period ( $t = 3000 \text{ s}$ ). In response to this, the cumulative energy consumption of the SOEC stack increases linearly with time and reaches 7.6 Wh at  $t = 3000 \text{ s}$ .

The upper limit of the compressor power,  $P_{\text{CPmax}}$ , is set to different values in the range of 3–16 W, corresponding to the air ratio range of 0.4–14, as calculated from Eqs. (1) and (2). In Fig. 7(b), one can see how the air ratio responds to the compressor power bounds: it rises at  $t = 1 \text{ s}$  from the initial value of 0.4 to the controlled values based on the compressor power bound, as current density changes from  $7000$  to  $1000 \text{ A m}^{-2}$ . For the range of air ratio values considered, the temperature difference between the outlet and inlet of a cell is controlled within the constraint  $|\Delta T_C| \leq 100 \text{ K}$  and reaches steady state towards the end of the control period ( $t = 3000 \text{ s}$ ), as shown in Fig. 7(c). The absolute value of the maximum local temperature gradient in the solid structure,  $|\partial T_S(x, t)/\partial x|$ , is observed to be under the 10 K bound for all the  $P_{\text{CPmax}}$  control cases as shown in Fig. 7(d). It is also obvious that with a small compressor power limit, a larger temperature difference is observed, and vice versa. For example, with  $P_{\text{CPmax}} = 16 \text{ W}$ , a high air ratio of 14 is introduced to the cathode stream of the SOEC stack, which enables only a slight change in temperature and keeps  $\Delta T_C \sim -46 \text{ K}$  through the entire control period; with  $P_{\text{CPmax}} = 3 \text{ W}$ , an air ratio of 2.71 is introduced, bringing the temperature difference of  $\Delta T_C = -46 \text{ K}$  to a constant value of  $-99.5 \text{ K}$  within 2500 s.

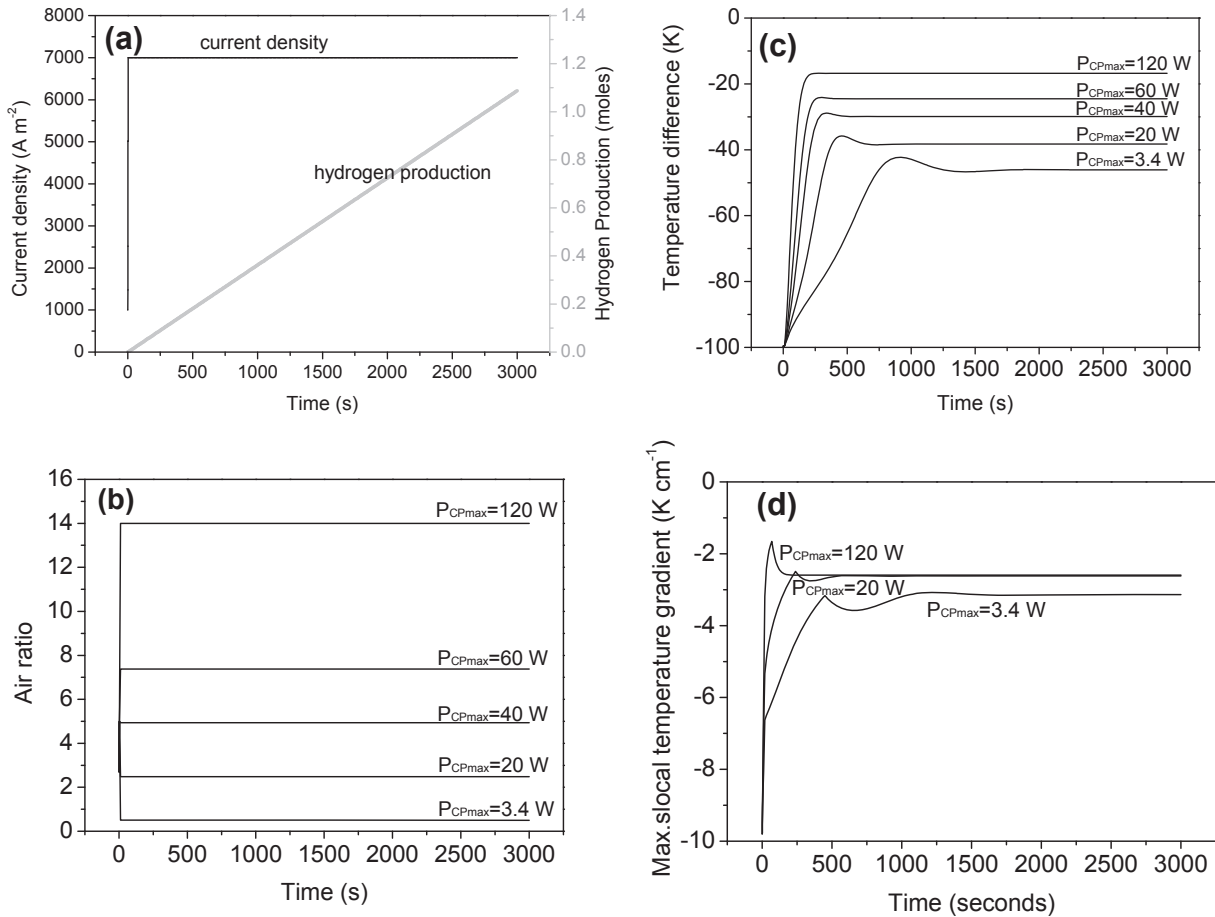


**Fig. 6.** Optimal profiles of (a) current density and hydrogen production, (b) air ratio, (c) cathode stream temperature difference and (d) maximum local temperature gradient in the solid structure, for the case of maximizing hydrogen production.

### 3.3. The effect of compressor power on hydrogen production and energy consumption

The results in the above two control cases (i.e. maximizing hydrogen production and minimizing the SOEC energy consumption) show that the control of the SOEC system illustrated in Fig. 1 is feasible as long as the compressor power limit is maintained within a reasonable range, under which the constraints become active; the impact of imposing a compressor power limit on the system affects the air flow rate, and consequently the temperature gradient  $\Delta T_C$  and the rate of the temperature gradient change with time  $\partial\Delta T_C/\partial t$ . When the power limit for the compressor is sufficiently large, the constraints become inactive. If a sufficiently large power limit is set on the compressor, the system will automatically choose to work under the biggest allowable air flow rate, bringing  $\Delta T_C$  and  $\partial\Delta T_C/\partial t$  down to very low values which benefit the materials of the SOEC stack.

However, the power limit imposed on the compressor needs to be set considering other factors such as the system energy consumption. The effects of the compressor power limit on both energy consumption and hydrogen production of the SOEC system are further explored. Fig. 8(a) and (b) shows the total hydrogen production and energy consumption over the entire time horizon of 3000 s, as a function of the maximum compressor power,  $P_{CPmax}$ , for both maximizing hydrogen production and minimizing the SOEC energy consumption. As can be seen from Fig. 8(a) and (b), the total amount of hydrogen produced does not change with the variation in compressor power, as expected. According to Faraday's

law of electrolysis, the amount of hydrogen produced through an electrolysis process depends only on current density, as stated in Eq. (5). Since the implementation of the compressor power limit has no effect on the current density profiles, the variation in compressor power is not expected to affect the amount of hydrogen produced.

$$m_{\text{H}_2}(t) = \frac{Q}{nF} = \frac{\int_{t=0}^{t=t_f} \bar{j}(t) dt}{nF} \quad (5)$$

The total amount of hydrogen produced over 3000 s is 1.09 mol in the case of maximizing hydrogen production, and 0.16 mol in the case of minimizing SOEC energy consumption. These two extreme cases provide useful quantitative information on the range of possible behaviours of the system. The objective of maximizing hydrogen production gives a hydrogen production seven times larger than when minimizing energy consumption.

For both optimal control strategies, the total energy consumption of the SOEC system (which includes the SOEC stack and the compressor) per unit hydrogen production increases linearly with increasing compressor power limit,  $P_{CPmax}$ . The increase in the total energy consumption is mainly due to the increase in the compressor energy consumption because a higher  $P_{CPmax}$  allows for a higher air ratio and thus a higher  $P_{CP}$  according to Eqs. (1) and (2). The energy consumption of the SOEC stack per unit of hydrogen production only decreases slightly with an increase in the compressor power limit  $P_{CPmax}$ . This is because the bound on the

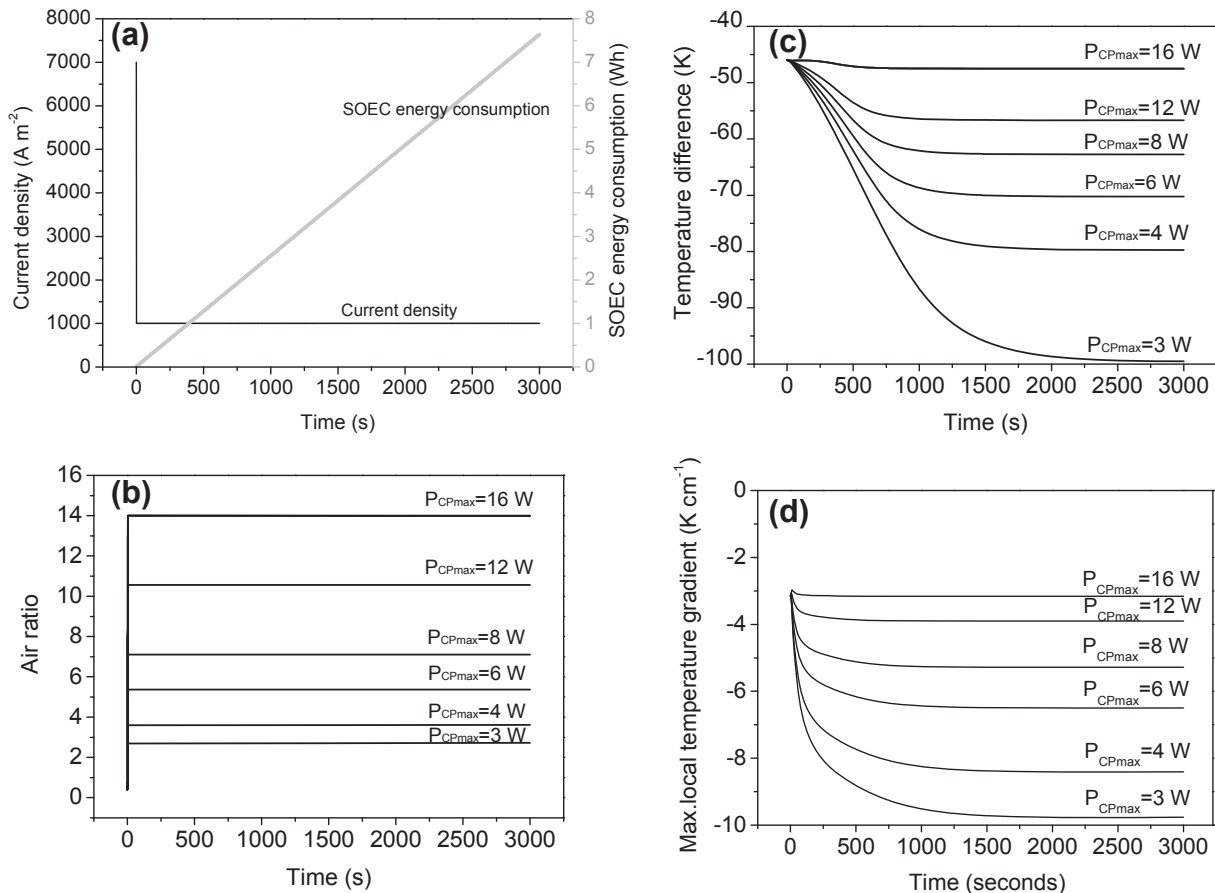


**Fig. 7.** Optimal profiles of (a) current density and SOEC energy consumption, (b) air ratio, (c) temperature difference and (d) maximum local temperature gradient in the solid structure, in the case of minimizing energy consumption of the SOEC stack.

compressor power does not have any effect on the current density profile, but only has a minor effect on cell voltage, with a higher air ratio (as a result of a higher  $P_{CPmax}$ ) giving a slightly lower cell voltage and in turn a slightly lower SOEC power demand. The gap between the SOEC energy consumption per unit hydrogen production  $E_{SOEC}$  and the total energy consumption per unit hydrogen production  $E_{total}$  becomes bigger at a larger compressor power limit. For example, in the case of maximizing hydrogen production as shown in Fig. 8(a), when a strict bound is imposed on the compressor power, at  $P_{CPmax} = 4$  W,  $E_{SOEC}$  is 96% of  $E_{total}$ , indicating that the SOEC stack is the dominant energy consumer; when a loose bound is imposed on the compressor power, at  $P_{CPmax} = 120$  W,  $E_{SOEC}$  is only 42% of  $E_{total}$ , meaning that compressor is the major energy consumer. The similar trend is observed with the case of minimizing the SOEC energy consumption. Therefore, from the energy saving point of view, one may choose to operate the system with a small compressor power limit.

On the basis of total energy consumption per unit hydrogen production, the control strategy of minimizing the SOEC energy consumption does not bring benefit, compared to the control strategy of maximizing hydrogen production. This is clearly shown in Fig. 8(a) and (b). For example, for the case of a strict compressor power bound when  $P_{CPmax} = 4$  W, the total energy consumption per unit hydrogen production in minimizing SOEC stack energy consumption is 72.48 Wh per mole  $H_2$ , compared to 70.76 Wh per mole  $H_2$  when maximizing hydrogen production at  $P_{CPmax} = 4$  W. For the case of a loose compressor power bound, the total energy consumption per unit hydrogen production when minimizing SOEC stack energy consumption at  $P_{CPmax} = 16$  W is 134.64 Wh per mole

$H_2$ , compared to 81.56 Wh per mole  $H_2$  when maximizing hydrogen production at  $P_{CPmax} = 16$  W. However, when these numbers are multiplied by the amount of hydrogen produced, the total energy consumption at  $P_{CPmax} = 16$  W is 20.93 Wh for minimum SOEC stack energy consumption, and 88.7 Wh for maximum hydrogen production, showing a much larger energy consumption in the latter case.

The choice of control strategy is thus a matter of priority, depending on whether the amount of hydrogen produced is the main concern, or the amount of energy consumed. Such a choice will automatically depend on factors such as location, season, electricity price and hydrogen price, etc. For example, one may want to operate the SOEC system by switching between the two control situations; maximizing hydrogen production when surplus electricity from intermittent energy sources is abundant and the electricity price is relatively low, and minimizing SOEC electricity consumption at times when little surplus electricity from intermittent energy sources is available and the electricity price is high.

### 3.4. Minimizing energy consumption by the air compressor

In this section we look at Scenario B where the electricity input to the SOEC system (as illustrated in Fig. 1) acts as a disturbance, to mimic the variations of power over time found with intermittent renewable energy sources such as wind and solar energy. The variations of power from these energy sources can occur at all timescales: seconds, minutes, hours, days, months, seasons and years. Electrical power systems can be designed to cope effectively with these variations for optimal utilization of the power, and can

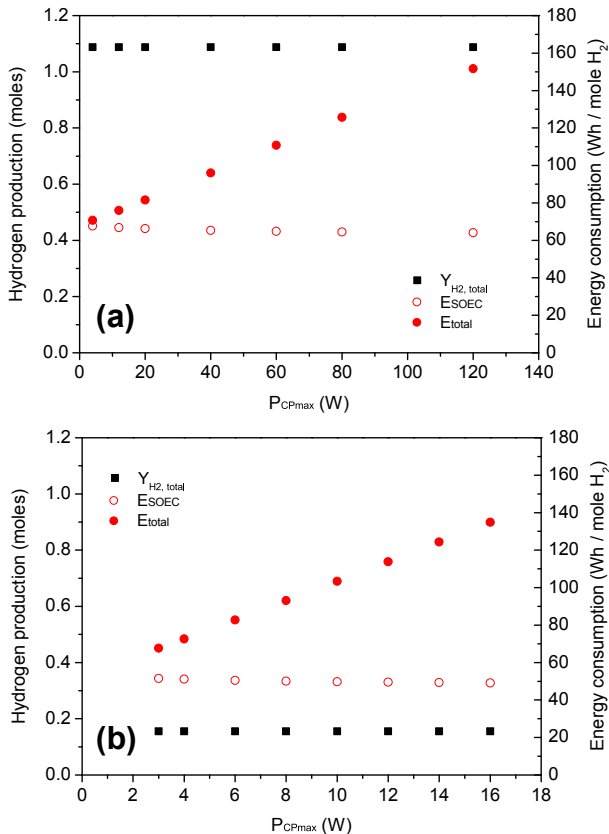


**Fig. 8.** Hydrogen production and energy consumption as a function of maximum compressor power in the case of (a) maximizing hydrogen production and (b) minimizing electrical energy consumption of the SOEC stack.

provide relatively smooth power [27]. It should be noted that we are not trying to simulate the 'real' fluctuations in power supply in this paper, but rather to study the feasibility of different control strategies for the SOEC system when there are fluctuations in electricity supply. For this purpose, the electricity disturbance in the power supply is arbitrarily simulated as step-wise constant profile that reaches a peak and then declines. The time horizon is chosen to be 3000 s, to be consistent with the optimal control studies for Scenario A, and also to represent the variations in power within a one-hour timeframe, as these have the most significant impact on the system from the technological point of view [28]. In Fig. 9, such a simulated peak with five time intervals,  $t_1$ – $t_5$ , is shown; the power increases from 20 W to 100 W, and then decrease to 20 W, in equal increments of 40 W.

In order to understand the impact of the input power disturbances on the SOEC system, three power profiles with different shapes (named as  $c1$ ,  $c2$  and  $c3$ ), shown in Fig. 9, are simulated and used in minimizing the compressor energy consumption. All three power profiles have step profiles starting at 20 W and reaching a maximum at 100 W. The first and the last intervals are kept the same for all the three power profiles, whilst the three intervals in the middle vary in duration, resulting in power profiles with narrower ( $c2$ ) to broader ( $c3$ ) peaks.

For a given input power profile, we set the optimal control objective to minimize the compressor energy consumption, which in turn will lead to the energy consumption and therefore hydrogen production of the SOEC stack being maximized. Fig. 10(a)–(f) shows the optimal control profiles when  $c1$  in Fig. 9 is input as the total power of the SOEC system. The optimal control profiles with power profiles  $c2$  and  $c3$  are not reported here as they have very similar

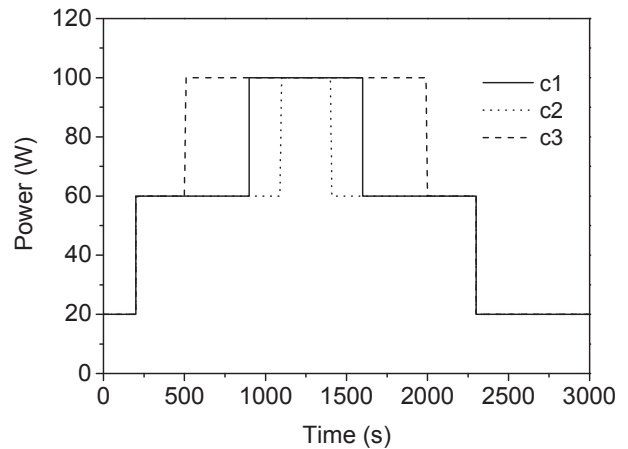


**Fig. 9.** The simulated electrical power profiles input to the SOEC system.

shapes as those for  $c1$ , shown in Fig. 10. As can be seen from Fig. 10(a), by minimizing the compressor energy consumption, the majority of the input power flows to the SOEC stack. The power profile of the SOEC stack in turn determines the current density profile, with similar step changes in the range of  $1430$ – $7600$  A  $m^{-2}$ , as shown in Fig. 10(b). The air ratio decreases from the initial value of 3.6, reaching its minimum value of 0.4 once the current density increases to  $4700$  A  $m^{-2}$  at  $t = 200$  s, and staying constant at 0.4 for most of the control period and then increasing again when the current density drops from  $4700$  to  $1600$  A  $m^{-2}$  at  $t = 2300$  s, in order to maintain the temperature difference and gradients within the constraints specified, as shown in Fig. 10(c). The temperature difference  $\Delta T$  rises gradually from  $\Delta T = -87.1$  K at the start to  $\Delta T = -31.5$  K at the peak, and then gradually falls to  $\Delta T = -88.6$  K at the end of the time horizon, as shown in Fig. 10(d). The maximum local temperature gradient in the solid structure, however, shows more fluctuation with time, as shown in Fig. 10(e); the highest gradient is found to be  $10$  K  $cm^{-1}$  when the current density drops from  $4700$  to  $1600$  A  $m^{-2}$ ; the lowest gradient is  $2.5$  K  $cm^{-1}$  during the interval when the current density is kept constant at  $7600$  A  $m^{-2}$ . The cumulative hydrogen production profile in Fig. 10(f) shows a non-linear increase with time; the total amount of hydrogen produced over the entire time horizon is 0.69 mol.

The amount of hydrogen produced and the energy consumption over the entire time horizon are summarized in Table 5 for all the three input power profiles  $c1$ – $c3$ . From Table 5 we can see that the lowest hydrogen production and lowest energy consumption (in terms of both total and per unit hydrogen production) are found with the input power profile  $c2$ ; whilst the highest hydrogen production and the highest energy consumption (in terms of both total and per unit hydrogen production) are found with the total input power profile  $c3$ .

For all the  $c1$ – $c3$  cases investigated here, the SOEC energy consumption is around 33 kWh per kg  $H_2$ , and the total energy consumption per unit hydrogen production is around 35 kWh per kg  $H_2$ . To compare, the reported total energy consumption of Hydrogenics and Norsk Hydro's alkaline electrolyser system, and Proton's PEM electrolyzer system, including all the auxiliary units, are 53.84 kWh per kg  $H_2$  and 70.18 kWh per kg  $H_2$  respectively [29]. Realistically, the total energy consumption of the SOEC system is going to be higher than 35 kWh per kg  $H_2$ . This is because: (1) a considerable amount of energy is required to heat up the SOEC stack and run auxiliary units such as heat exchangers, which is not included in the SOEC system studied in this paper; (2) in reality, inhomogeneity occurs in the SOEC stack, normally with cells at

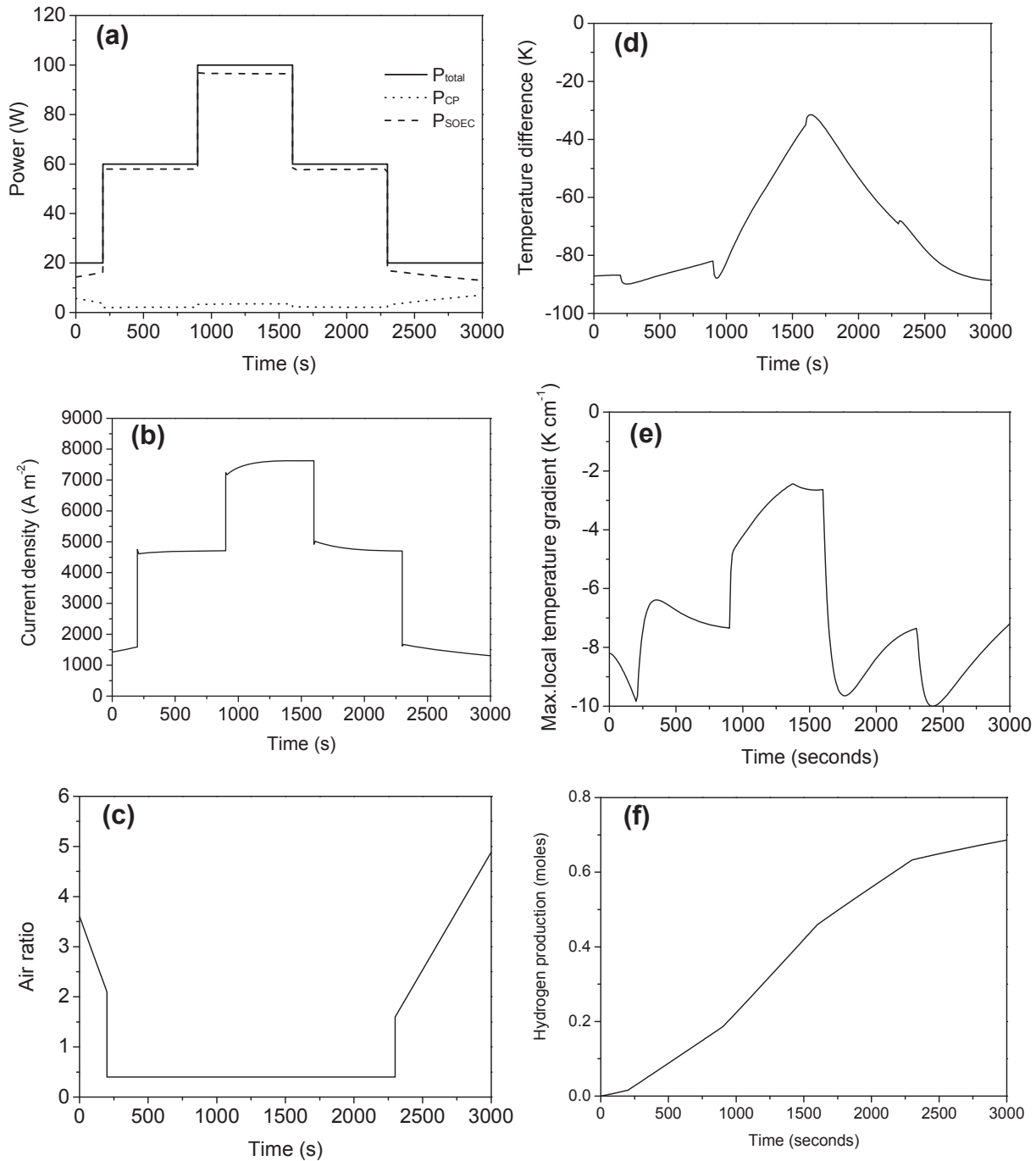


**Fig. 10.** Optimal profiles of (a) power, (b) current density, (c) air ratio, (d) temperature difference, (e) energy consumption, and (f) hydrogen production, in the case of minimizing compressor energy consumption for the total input power profile c1 (solid line in Fig. 9).

both ends having higher voltages (thus higher energy consumption) than those in the middle of the stack. Nevertheless, an energy consumption of 35 kWh per kg H<sub>2</sub> for an electrolyser system which includes the major energy consumption units (i.e. an SOEC and a compressor) is still competitive.

#### 4. Conclusions

A study of optimal control strategies for hydrogen production based on SOEC technology has been presented in this paper, with the aim of offering efficient large-scale system operation when

coupling an SOEC system with renewable energy sources. The system model used includes a 1D dynamic SOEC stack model and an air compressor model, to examine hydrogen production in relation to energy consumption. Several scenarios and optimal control strategies were considered: in Scenario A, in which the current density is a control variable allowed to vary over the range 1000–7000 A m<sup>-2</sup>, the impact of maximizing hydrogen production or minimizing SOEC energy consumption was considered. In Scenario B, in which the input power is treated as a disturbance, with a step-wise profile in the range of 20–100 W, the minimization of the air compressor energy consumption was investigated. Temperature

**Table 5**

Summary of hydrogen production and energy consumption for the control strategy discussed in Section 3.4.

	$Y_{H_2,\text{total}}$ (moles)	$E_{\text{SOEC}}$ (Wh)	$E_{\text{total}}$ (Wh)	$E_{\text{SOEC}} \text{ per kg H}_2$ ( $\text{kWh kg}^{-1} \text{H}_2$ )	$E_{\text{total}} \text{ per kg H}_2$ ( $\text{kWh kg}^{-1} \text{H}_2$ )
c1	0.69	45.02	47.78	32.62	34.62
c2	0.62	40.71	43.33	32.83	34.94
c3	0.81	53.52	56.67	33.04	34.98

control of the SOEC stack was imposed via path constraints for the overall temperature difference across the cell and the local temperature gradient, to link material properties with system performance. The optimal control profiles showed that these control strategies are feasible under a range of conditions. It was shown that it is important to impose a limit on the air compressor power in order to constrain the system energy consumption, when this is not considered in the objective function.

The two control strategies – maximizing hydrogen production and minimizing SOEC energy consumption – in Scenario A, were compared in terms of hydrogen production and energy consumption. As expected, the amount of hydrogen produced within the control horizon (3000 s) is much higher for maximizing hydrogen production than that for minimizing SOEC energy consumption. The energy consumption per unit hydrogen production (Wh per mole  $\text{H}_2$ ) for the two control strategies did not vary much. This provides guidance on what control strategy to choose depending on location, electricity price and hydrogen demand etc.

In Scenario B, when variation in the input power is introduced, the control strategy of minimizing compressor power was shown to have the expected effect of maximizing power sent to the SOEC stack, thus maximizing hydrogen production. Different power profiles were used as input to the SOEC system. The objective function chosen was found to ensure that the energy consumption per unit hydrogen production was very similar for the three different input power profiles considered. The energy consumption of the SOEC system studied was found to be 35 kWh per kg  $\text{H}_2$  in all cases. This is highly competitive with other methods of hydrogen production and provides a strong incentive for further development of SOEC based technologies for hydrogen production.

## Acknowledgement

Q. Cai is grateful for the funding support from the EPSRC (Engineering and Physical Sciences Research Council of UK) platform grant (EACPR PS0693) during this research.

## Appendix A. Supplementary data

Supplementary data related to this article can be found at <http://dx.doi.org/10.1016/j.jpowsour.2014.06.028>.

## Nomenclature

$c_{p,C}, c_{p,A}, c_{p,S}, c_{p,I}$	heat capacity of the cathode and anode gas streams, solid structure and interconnect ( $\text{J kg}^{-1} \text{K}^{-1}$ )
$c_{p,\text{air}}$	heat capacity of air ( $\text{J kg}^{-1} \text{K}^{-1}$ )
$C_{\text{H}_2}, C_{\text{H}_2\text{O}}, C_{\text{O}_2}, C_{\text{N}_2}$	concentration of hydrogen, steam, oxygen and nitrogen in the cathode and anode gas streams ( $\text{mol m}^{-3}$ )
$C_i$	concentration of gas species $i$ in the cathode and anode gas streams ( $\text{mol m}^{-3}$ )
$C_i^0, C_i^1$	concentration of gas species $i$ at the cell inlet and outlet ( $\text{mol m}^{-3}$ )

$C_{\text{H}_2}^{\text{TPB}}, C_{\text{H}_2\text{O}}^{\text{TPB}}, C_{\text{O}_2}^{\text{TPB}}$	concentration of hydrogen, steam and oxygen at the triple phase boundary ( $\text{mol m}^{-3}$ )
$d_{h,C}, d_{h,A}$	hydraulic diameter of the cathode and anode gas channels (m)
$D_{\text{eff,cathode}}, D_{\text{eff,anode}}$	average effective diffusivity coefficient of the cathode and anode ( $\text{m}^2 \text{s}^{-1}$ )
$E_{\text{electrode}}$	activation energy for the exchange current density of an electrode ( $\text{J mol}^{-1}$ )
$E_{\text{SOEC}}, E_{\text{CP}}$	energy consumption of the SOEC stack and the air compressor (kWh)
$f_A^0, f_C^0$	inlet flow rate of the anode and cathode streams ( $\text{mol s}^{-1}$ )
$F$	Faraday's constant ( $\text{C mol}^{-1}$ )
$h_C, h_A, h_S, h_I$	height of the cathode and anode channels, and thickness of the solid structure and interconnect (m)
$j(x)$	local current density in the $x$ direction ( $\text{A m}^{-2}$ )
$j_{0,\text{cathode}}, j_{0,\text{anode}}$	exchange current density of the cathode and anode ( $\text{A m}^{-2}$ )
$\bar{j}$	average current density of a cell ( $\text{A m}^{-2}$ )
$k_C, k_A$	convective heat transfer coefficient between the solid parts of the cell and the cathode and anode gas streams ( $\text{J m}^{-2} \text{s}^{-1} \text{K}^{-1}$ )
$k_{\text{electrode}}$	pre-exponential factor for the exchange current density of an electrode ( $\Omega^{-1} \text{m}^{-2}$ )
$L$	length of the SOEC stack in the $z$ direction (m)
$\dot{m}$	air flow rate into the compressor ( $\text{kg s}^{-1}$ )
$n$	the number of electrons transferred in an electrochemistry reaction, which is 2 for the steam electrolysis reaction
$Nu_C, Nu_A$	Nusselt number of the cathode and anode gas streams
$p_{\text{O}_2}$	oxygen pressure in the anode gas stream (Pa)
$p_{\text{air,out}}, p_{\text{air,in}}$	the outlet and inlet air pressure of the air compressor (Pa)
$P_{\text{SOEC}}, P_{\text{CP}}, P_{\text{total}}$	power input to the SOEC stack and the air compressor, and system total power demand (W)
$R$	reaction rate ( $\text{mol s}^{-1} \text{m}^{-2}$ )
$R_{\text{Ohm}}$	total resistance of the cell including electric and ionic resistances ( $\Omega \text{m}^2$ )
$\mathfrak{R}$	gas constant ( $\text{J mol}^{-1} \text{K}^{-1}$ )
$t$	time (s)
$t_f$	optimal control time horizon (s)
$T$	temperature (K)
$T_C, T_A, T_S, T_I$	temperature of the cathode and anode gas streams, solid structure and interconnect (K)
$T_C^0, T_C^1$	temperature of the cathode gas stream at the inlet and the outlet (K)
$u_C, u_A$	velocity of the cathode and anode gas streams ( $\text{m s}^{-1}$ )
$U$	cell potential (V)
$U^0$	standard potential (V)
$U^{\text{rev}}$	reversible potential (V)
$U^{\text{rev,TPB}}$	reversible potential estimated for the gas concentrations at the triple phase boundary (V)
$w$	width of a cell in the $x$ direction (m)
$x$	axial coordinate (m)
$Y_{\text{O}_2}$	mole fraction of oxygen in the anode gas streams
$\dot{Y}_{\text{H}_2}$	hydrogen production rate per ( $\text{mol s}^{-1}$ )
$Y_{\text{H}_2,\text{total}}$	total hydrogen production over the entire control time horizon (mol)
$\alpha$	transfer coefficient
$\gamma$	ratio of the specific heat of air $\gamma = 1.4$
$\epsilon_S, \epsilon_I$	emissivity of the solid structure and interconnect
$\eta_{\text{act,cathode}}, \eta_{\text{act,anode}}$	activation overpotential losses at the cathode and anode (V)
$\eta_{\text{conc,cathode}}, \eta_{\text{conc,anode}}$	concentration overpotential losses at the cathode and anode (V)

$\eta_{\text{ohm}}$	Ohmic losses (V)
$\eta_{\text{CP}}, \eta_{\text{EM}}$	compressor efficiency and compressor drive motor efficiency
$\lambda_C, \lambda_A, \lambda_S, \lambda_I$	thermal conductivity of the cathode and anode gas streams, solid structure and interconnect ( $\text{J m}^{-1} \text{s}^{-1} \text{K}^{-1}$ )
$\nu_i$	stoichiometric coefficient of gas species $i$
$\nu_{\text{O}_2}$	stoichiometric coefficient of oxygen
$\rho_C, \rho_A, \rho_S, \rho_I$	density of the cathode and anode gas streams, solid structure and interconnect ( $\text{kg m}^{-3}$ )
$\rho_{\text{air}}$	density of air ( $\text{kg m}^{-3}$ )
$\sigma$	Stefan–Boltzmann constant ( $\text{W m}^{-2} \text{K}^{-4}$ )
$\sigma_{\text{cathode}}, \sigma_{\text{anode}}$	electric conductivity of the cathode and anode ( $\Omega^{-1} \text{m}^{-1}$ )
$\sigma_{\text{electrolyte}}$	ionic conductivity of the electrolyte ( $\Omega^{-1} \text{m}^{-1}$ )
$\tau_{\text{cathode}}, \tau_{\text{electrolyte}}, \tau_{\text{anode}}$	thickness of the cathode, electrolyte and anode (m)
$\psi$	air ratio

## References

- [1] REN 21, Renewables, Global Status Report, Available:, 2013 <http://www.ren21.net/REN21Activities/GlobalStatusReport.aspx>.
- [2] M.N. Manage, D. Hodgson, N. Milligan, S.J.R. Simons, D.J.L. Brett, Int. J. Hydrogen Energy 36 (2011) 5782–5796.
- [3] M.A. Laguna-Bercero, J. Power Sources 203 (2012) 4–16.
- [4] J. Scheffold, A. Brisse, F. Tietz, J. Electrochem. Soc. 159 (2012) A137–A144.
- [5] M.A. Laguna-Bercero, S.J. Skinner, J.A. Kilner, J. Power Sources 192 (2009) 126–131.
- [6] A. Brisse, J. Scheffold, M. Zahid, Int. J. Hydrogen Energy 33 (2008) 5375–5382.
- [7] P.A. Stuart, T. Unnоб, J.A. Kilner, S.J. Skinner, Solid State Ionics 179 (2008) 1120–1124.
- [8] M.A. Azimova, S. McIntosh, Solid State Ionics 203 (2011) 57–61.
- [9] M.A. Laguna-Bercero, V.M. Orera, Int. J. Hydrogen Energy 36 (2011) 13051–13058.
- [10] C.J. Moyer, N.P. Sullivan, H. Zhu, R.J. Kee, J. Electrochem. Soc. 158 (2011) B117–B131.
- [11] S. Pati, S. Gopalan, U.B. Pal, Int. J. Hydrogen Energy 36 (2011) 152–159.
- [12] P. Kim-Lohsoontorn, D.J.L. Brett, N. Laosiripojana, Y.-M. Kim, J.-M. Bae, Int. J. Hydrogen Energy 35 (2010) 3958–3966.
- [13] G. Schiller, A. Ansar, M. Lang, O. Patz, J. Appl. Electrochem. 39 (2009) 293–301.
- [14] M. Ni, M.K.H. Leung, D.Y.C. Leung, Electrochim. Acta 52 (2007) 6707–6718.
- [15] D. Grondin, J. Deseure, A. Brisse, M. Zahid, P. Ozil, J. Appl. Electrochem. 40 (2009) 933–941.
- [16] J. Udagawa, P. Aguiar, N.P. Brandon, J. Power Sources 180 (2008) 354–364.
- [17] J. Udagawa, P. Aguiar, N.P. Brandon, J. Power Sources 180 (2008) 46–55.
- [18] J. Laurencin, D. Kane, G. Delette, J. Deseure, F. Lefebvre-Joud, J. Power Sources 196 (2011) 2080–2093.
- [19] G. Hawkes, J. O'Brien, C. Stoots, B. Hawkes, Int. J. Hydrogen Energy 34 (2009) 4189–4197.
- [20] X.W. Zhang, S.H. Chan, H.K. Hob, J. Lia, G. Lia, Z. Feng, Int. J. Hydrogen Energy 33 (2008) 2355–2366.
- [21] S.-R. Oh, J. Sun, H. Dobbs, J. King, J. Fuel Cell Sci. Technol. 8 (2011) 0610201–06102012.
- [22] M. Sorrentino, C. Pianese, J. Power Sources 196 (2011) 9036–9045.
- [23] Y. Li, J. Shen, J. Lu, J. Power Sources 196 (2011) 5873–5880.
- [24] J.E. O'Brien, M.G. McKellar, E.A. Harvego, C.M. Stoots, Int. J. Hydrogen Energy 36 (2010) 4808–4819.
- [25] Q. Cai, E. Luna-Ortiz, C.S. Adjiman, N.P. Brandon, Fuel Cells 10 (2010) 1114–1128.
- [26] P. Aguiar, C.S. Adjiman, N.P. Brandon, J. Power Sources 147 (2005) 136–147.
- [27] V.S. Vassiliadis, R.W.H. Sargent, C.C. Pantelides, Ind. Eng. Chem. Res. 33 (1994) 2111–2133.
- [28] P. Sørensen, N.A. Cutululis, A. Vigueras-Rodríguez, L.E. Jensen, J. Hjerrild, M.H. Donovan, IEEE Trans. Power Syst. 22 (2007) 958–965.
- [29] J. Ivy, Summary of Electrolytic Hydrogen Production: Milestone Completion Report, National Renewable Energy Laboratory, Colorado, 2004.